Applied Catalysis B: Environmental 318 (2022) 121886

Contents lists available at ScienceDirect

Applied Catalysis B: Environmental

journal homepage: www.elsevier.com/locate/apcatb

Impact of nanoparticle exsolution on dry reforming of methane: Improving catalytic activity by reductive pre-treatment of perovskite-type catalysts

F. Schrenk [a], L. Lindenthal [a], H. Drexler [a], G. Urban [a], R. Rameshan [a,b], H. Summerer [b], T. Berger [a], T. Ruh [a], A.K. Opitz [b], C. Rameshan [a,*]

[a] TU Wien, Institute of Materials Chemistry, Getreidemarkt 9/165-PC, 1060 Vienna, Austria
[b] TU Wien, Institute of Chemical Technologies and Analytics, Getreidemarkt 9/164-EC, 1060 Vienna, Austria

ARTICLE INFO

Keywords:
Perovskite
Exsolution
Coke resistance
in-situ NAP-XPS
CO_2 utilisation

ABSTRACT

Nanoparticle exsolution is regarded as a promising alternative to classical catalyst synthesis routes. In this work, we compare the catalytic performance of nanoparticles formed by *in-situ* exsolution during dry reforming of methane with particles pre-formed by reductive pre-treatment. The experiments were conducted on three perovskite-type oxides. Using a combination of *in-situ* and *operando* spectroscopic investigations (x-ray diffraction, near ambient pressure x-ray photoelectron spectroscopy) and the correlation to the obtained catalytic results, we could highlight that pre-formed nanoparticles strongly enhance the activity compared to *in-situ* exsolution. Scanning electron microscope images recorded after catalytic tests revealed that nanoparticles formed during reductive pre-treatment are bigger on average than particles formed *in-situ*. Furthermore, B-site doping with Co or Ni significantly enhanced the catalytic activity. Importantly, the perovskite host lattice was stable in all experiments, thus providing the necessary enhanced oxygen surface chemistry which is the key to the coking resistance of the investigated materials. Additionally, we observe a temperature dependent change of mechanism leading to different product ratios.

1. Introduction

Dry Reforming of Methane (DRM) has great potential to contribute to current efforts towards a sustainable energy future. Beyond that, this catalytic reaction turns two of Earth's most abundant greenhouse gases, CO_2 and CH_4, into valuable synthesis gas [1], thus mitigating global warming. Both products of DRM, H_2 and CO, are building blocks in the synthesis of various fuels and chemicals via heterogeneous catalysis, e.g. generation of hydrocarbons via Fischer-Tropsch synthesis or methanol production [2,3]. Especially the Fischer-Tropsch reaction benefits from the low H_2/CO ratio obtained by DRM [4]. DRM is represented by following Eq. (1):

$$CH_{4(g)} + CO_{2(g)} \rightleftharpoons 2H_{2(g)} + 2CO_{(g)} \quad (\Delta H_r^{298} = +247 kJmol^{-1}) \tag{1}$$

The endothermic nature of DRM necessitates high operating temperatures in order to achieve high conversions, usually between 650 °C and 1000 °C [5]. Unfortunately, DRM is still not a mature industrial process, despite its great environmental potential [4]. High operating temperatures and associated deactivation phenomena of sintering and coke formation are the biggest obstacles. Steam reforming, partial oxidation, or autothermal reforming of methane are the dominant technologies for syngas production from methane on an industrial level; however, they mainly yield hydrogen-rich products [6]. In contrast, due to the introduction of an additional carbon source, DRM leads to CO-rich syngas, beneficial for certain downstream processes (e.g. production of acetic acid [6]). Consequently, the interest in DRM is still extremely high, and further developments are necessary to obtain effective catalyst materials that are stable at the required operation temperatures.

Various catalyst materials have been extensively studied for their capability of promoting DRM, with Ni-supported catalysts mostly utilised for industrial processes due to their high activity and low cost [7,8]. Unfortunately, they suffer from deactivation by carbon deposition and/or Carbon Nano Tube (CNT) formation [9]. Noble metal-based materials (e.g. Pt, Pd, Rh, Ru…) are less prone to such adverse side reactions, although their expensive nature makes them unsuitable for large-scale applications [1,5]. By adding small amounts of noble metals to e.g. Ni-based catalysts with subsequent alloy formation, both drawbacks, carbon formation and high cost, can be alleviated [10].

* Corresponding author.
E-mail address: christoph.rameshan@tuwien.ac.at (C. Rameshan).

https://doi.org/10.1016/j.apcatb.2022.121886
Received 17 May 2022; Received in revised form 11 August 2022; Accepted 20 August 2022
Available online 24 August 2022

Furthermore, use of bimetallic catalysts enables tuning of particle size and dispersion, thus increasing overall performance [11]. Wang et al. calculated the thermodynamically limiting temperatures in DRM for carbon formation (carbon is not stable above this limit) as a function of the educt ratio and found that in a CO_2 excess this temperature decreases, meaning that this excess can prevent carbon formation at temperatures below 700 °C [12]. During the search for highly active materials, Co- and Fe-based materials were tested as well [9,13] with Co reaching almost the activity level of Ni [4]. Moreover, perovskite-type materials have lately drawn much attention as promising substitutes to conventional catalysts, as they allow a design approach, making cost effective and highly active materials available. For example, Dama et al. have demonstrated high performance for $CaZr_{0.8}Ni_{0.2}O_{3-\delta}$ [14]. Additionally, perovskites are often used as precursors for DRM catalysts that release the active metal upon reductive treatment, which is accompanied by partial decomposition of the perovskite into the respective oxides [15,16]. Unfortunately, the rich redox and defect chemistry of the perovskite surface – which is highly beneficial for DRM – is lost during this process.

Although numerous studies in the past intensively investigated DRM on supported metal catalysts, the reaction mechanism is still debated without general agreement [17]. One reason for this may be related to the fact that the mechanism depends significantly on the utilised materials and the combination of active metal and nature of the oxide support [6,18]. In principle, the reaction mechanism can be divided in the following major steps: The first step is the dissociative adsorption of methane, which occurs on the metal and is established as the rate limiting step for e.g. Ni [4]. Dissociative adsorption of CO_2 occurs in parallel on the surface of the support, which is considered a fast reaction step. It has to be emphasised that CO_2 activation is strongly dependent on the used materials, with basic or redox-active supports or surface defects strongly enhancing this process (e.g. oxygen vacancies on perovskite surfaces are extremely active for CO_2 activation already at low temperatures around 400 °C) [14,19]. In a subsequent reaction step, the formed H from CH_4 dissociation can either desorb as H_2 or move to the support to form OH-groups that can be observed below 800 °C [4]. In the latter case, a competing reverse Water Gas Shift (rWGS) type reaction is dominating – especially as it is thermodynamically favoured compared to the DRM-pathway at lower reaction temperatures. Both pathways result in the formation of NiO and NiC which can recombine and lead to the desorption of CO. These two possible pathways are depicted in Fig. 1. OH-groups can react with activated CO_2 (forming e.g. formate) or with CH_x groups to form CH_xOH. The most complex part of the reaction mechanism is the oxidation of the intermediates and the subsequent CO and H_2 desorption with many different possible pathways reported in literature. For instance, Iglesia and Wei outlined different routes of CH_x oxidation via surface oxygen [20]. Most models were established for Ni-based materials, but they are claimed to be transferable to noble metal systems in literature (Wittich et al. [6].)

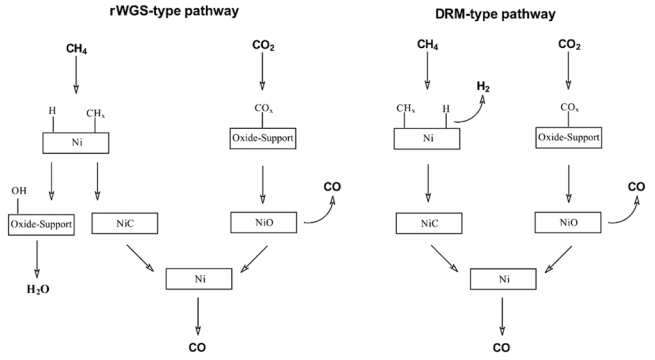

Fig. 1. Comparison between two possible pathways with different reactions of the adsorbed hydrogen according to literature. On the left, the "rWGS-type pathway" is shown, where the adsorbed hydrogen spills over to the support, subsequently forming OH-groups, which in turn can combine and desorb as H_2O. On the right, the "DRM-type pathway" is depicted, where the adsorbed hydrogen atoms recombine directly, subsequently forming H_2 which desorbs.

The H_2/CO ratio obtained by DRM (which ideally should be 1, according to Eq. 1) depends strongly on the reaction temperature: the rWGS-type pathway occurs under similar reaction conditions and reduces the ratio as can be seen in the rWGS equation:

$$H_{2(g)} + CO_{2(g)} \rightleftharpoons H_2O_{(g)} + CO_{(g)} \quad (\Delta H_r^{298} = +42.1 kJmol^{-1}) \tag{2}$$

Aside from rWGS, a large number of additional possible side reactions influence the DRM process, a brief summary of which is given by Aramouni et al. [4]. Higher operating temperatures are generally favourable for DRM, as CO and CO_2 hydrogenation or the Boudouard reaction, for example, occur at lower reaction temperatures. The latter, together with methane dehydrogenation, which is more pronounced at high reaction temperatures (>730 °C), is the main source for carbon deposition on DRM catalysts. The degree of catalyst deactivation by coking depends on the utilised materials. The choice of support has a strong influence on coking resistance, with highly redox-active oxides promoting the removal of formed carbon deposits during DRM [5,14]. Basic oxides and perovskites have been reported to exhibit increased ability for carbon gasification [21]. Perovskites in particular are promising alternatives due to their rich surface redox chemistry and thermal stability [19]. In addition, perovskites provide the opportunity to incorporate dopant materials on both A- and B-site, enabling the synthesis of materials that contain additional promoters and catalytically active elements. For instance, addition of Ca to DRM catalysts has been reported to improve carbon removal from the surface [14].

Doping Ni or Co on the B-site of perovskites leads to the formation of metallic nanoparticles upon reduction or in reducing reaction environments via exsolution as was reported previously [22]. Unlike the precursor method mentioned above, exsolution preserves the perovskite structure – meaning its beneficial properties are not lost. Due to their high dispersion and strong anchoring to the surface, the metallic nanoparticles provide an ideal system for DRM. Additionally, Neagu et al. showed that small nanoparticles (around 20 nm) that were produced via exsolution are still stable in high temperature reducing conditions, even though the surface area of the perovskite was around 1 $m^2 g^{-1}$ [23]. High metal dispersion in combination with available surface oxygen enhances coking resistance of these type of system as reported by Dama et al. [14].

This was the motivation to use Co- and Ni-doped perovskites for the present study, which was focussed on comparing the effect of the formation of the metal nanoparticles during DRM (*in-situ* exsolution) to the effect of pre-reduction with H_2/H_2O (with the formation of the nanoparticles prior to the catalytic reactions). Both phenomena were studied by catalytic testing as well as with *in-situ* surface chemical analysis by Near Ambient Pressure X-Ray Photoelectron Spectroscopy (NAP-XPS) and *operando* X-Ray Diffraction (XRD). For this purpose, perovskites with the nominal compositions $Nd_{0.6}Ca_{0.4}FeO_{3-\delta}$ (B-site undoped), $Nd_{0.6}Ca_{0.4}Fe_{0.9}Co_{0.1}O_{3-\delta}$ (B-site Co-doped), and $Nd_{0.6}Ca_{0.4}Fe_{0.97}Ni_{0.03}O_{3-\delta}$ (B-site Ni-doped) were investigated. The obtained results were supplemented by Scanning Electron Microscopy (SEM) combined with Energy Dispersive X-Ray analysis (EDX).

2. Experimental methods

2.1. Sample preparation

The catalysts ($Nd_{0.6}Ca_{0.4}FeO_{3-\delta}$, $Nd_{0.6}Ca_{0.4}Fe_{0.9}Co_{0.1}O_{3-\delta}$, and $Nd_{0.6}Ca_{0.4}Fe_{0.97}Ni_{0.03}O_{3-\delta}$) were prepared via a modified Pechini synthesis method, as outlined in detail in previous works [22,24]. To that end, the respective starting materials Nd_2O_3 (99.9 %, Strategic Elements), $CaCO_3$ (99.95 %, Sigma-Aldrich), Fe (99.5 %, Sigma-Aldrich),

$Ni(NO_3)_3 0.6\ H_2O$ (98 %, Alfa Aesar), and $Co(NO_3)_3 0.6\ H_2O$ (99.999 %, Sigma-Aldrich) were mixed in stochiometric amounts and dissolved in either HNO_3 (65 % Merck) or H_2O, both doubly distilled. The salts were complexed using citric acid (99.9998 % trace metal pure, Fluka) in excess of 20 mol% with regard to the cations. After evaporation of the liquid on a heater, the resulting gels were ignited by further heating, leading to the formation of powders. These powders were calcined for 3 h at 800 °C. The catalyst $Nd_{0.6}Ca_{0.4}Fe_{0.97}Ni_{0.03}O_{3-\delta}$ had a reduced Ni content and underwent an additional annealing step at 1200 °C, as phase impurities were observed even after the calcination step of the original synthesis. The products were ground to ensure homogeneity. Respective surface areas and morphological characterisation of the pristine perovskites can be found in reference [22]. The weights used for the synthesis are listed in the Supporting Information (SI) in Tables S1 to S3.

2.2. Structural and morphological characterisation

The powder XRD measurements were carried out on a PANalytical X'Pert Pro diffractometer (Malvern Panalytical, Malvern, UK) in Bragg-Brentano geometry using a mirror for separating the Cu $K_{\alpha 1,2}$ radiation and an X'Celerator linear detector (Malvern Panalytical, Malvern, UK). For the *operando* experiments, an Anton Paar XRK 900 chamber (Anton Paar, Graz, Austria) was used. After sample preparation, the catalysts were pre-treated with oxygen (600 °C, 40 min, 0.5 L min^{-1} O_2) before switching to the reaction atmosphere. The DRM reaction was carried out in CH_4 excess (48 mL min^{-1} CH_4, 16 mL min^{-1} CO_2, and 50 mL min^{-1} Ar at ambient pressure) at increasing temperatures (going from 300 °C to 700 °C with 50 °C steps). The methane excess was chosen for two reasons: Firstly, to simulate real biogas conditions, as – dependent on the feedstock – biogas generally consists of around 66 % CH_4 and 32 % CO_2 [25,26]. Secondly, CH_4 excess leads to a reducing atmosphere and, therefore, may promote *in-situ* exsolution. At each step, reaction conditions were held for 10 min (to achieve equilibrium) before an *operando* XRD measurement (about 30 min) was carried out. For interpretation of the data and assignment of the diffraction peaks, the PDF-4 + 2019 database (International Centre for Diffraction Data) [27] in combination with the HighScore Plus [28] software (PANalytic) was used. Assignment was performed by comparison with database structures and measurements and validated by performing Rietveld refinements.

A Quanta 250 FEGSEM (FEI Company) microscope was used to record SEM images for morphology examination. Additionally, EDX was performed with an Octane Elite X-Ray detector (EDAX Inc). To obtain a satisfactory surface sensitivity, an acceleration voltage of 5 kV was used for imaging and of 10 kV for EDX measurements.

In-situ NAP-XPS experiments were performed on 200 nm thick catalyst films, which were grown on Yttria Stabilised Zirconia (YSZ) single crystals in (100) orientation with a size of 5×5x 0.5 mm (CrysTec) via **P**ulsed **L**aser **D**eposition (PLD). The detailed manufacturing process is described in the SI and in previous work [24]. The exact setup of the samples as well as the NAP-XPS sample stage is described in previous work as well [29]. Monochromatic Al K_α radiation with a spot size of 350 μm was used for excitation achieving an energy resolution of around 0.2 eV. Heating was done using a near-IR laser with a wavelength of 970 nm and a maximum output of 100 W, the temperature was monitored with a S-type thermocouple mounted on the sample stage as well as a pyrometer (LumaSense Technology). Both temperature measurement methods were previously calibrated utilising electrochemical impedance spectroscopy and the known temperature dependent resistivity of the YSZ substrate. Therefore, the high frequency offset could be attributed to the ohmic resistance of YSZ, which then was used to calculate the temperature [30]. Similar to the other experiments, all catalysts were initially oxidised in 1 mbar of O_2 at 600 °C. NAP-XPS spectra of all relevant core levels including carbon, sulphur, and the fermi edge were recorded simultaneously. After ensuring equal initial states for all samples, the gas phase was changed to reaction conditions (CH_4:CO_2 = 2:1) at a total pressure of 1 mbar. The reaction temperature was increased in steps of 50 °C from 400 °C to 700 °C. At each step, a full set of spectra was collected (survey, Nd4d, Ca2p, Fe2p, Co2p, Ni2p, O1s, C1s, S2p, fermi edge). To evaluate the recorded XPS spectra, the software Casa XPS was employed. The background was approximated with a Shirley background and binding energies were calibrated using a combination of the Fermi edge and the $Ca2p^{3/2}$ peak (364.1 eV). The peaks were fitted with a "Gaussian/Lorentzian product form 30″ function as implemented in Casa XPS ("GL(30)") without asymmetry restriction. Two constraints were applied to the fits of the Ca2p spectra: the difference in binding energy between $2p^{1/2}$ and $2p^{3/2}$ was fixed at 3.55 eV, and the area ratio of the $2p^{1/2}$ and the $2p^{3/2}$ was set to 1:2. Fe2p spectra were fitted with four components, namely Fe(II) and Fe(III) for the $2p^{1/2}$ and $2p^{3/2}$ transition each. Spin orbit splitting for the $2p^{1/2}$ and $2p^{3/2}$ fits were set to 13.6 eV and the difference in binding energy was fixed at 1.5 eV between Fe(II) and Fe(III). For the area ratio of the Fe $2p^{1/2}$ and $2p^{3/2}$ transition, a fixed value of 0.4:1 was used. This deviates from the theoretical value of 0.5:1, but results in a better fit most likely due to uncertainties in the background determination.

2.3. Catalytic experiments

To test the activity of the catalysts, a fixed bed reactor system operating at ambient pressure was used as described in previous works [22,24]. In short, it consists of a home-built gas mixing system made from steel tubes (Burde & Co, Vienna, Austria) and fittings (Swagelok, Solon, USA) and an optional saturator filled with water. The catalyst is fixed in a quartz glass tube with 6 mm diameter (4 mm inner diameter) in an oven, and a Micro-**G**as **C**hromatography system (Micro-GC, Fusion 3000 A, Inficon) is used to analyse the gas composition of the reaction gas mixture after passing through the reactor every 2–3 min to monitor the catalytic activity. The amounts of the catalysts were chosen in such a way to yield conversions between 10 % and 20 % at 700 °C, ensuring that the thermodynamic equilibrium is not reached. The K-type thermocouple was placed inside the catalyst bed to ensure that measured temperature matches the actual temperature of the catalyst. To achieve comparable starting conditions for all catalysts, an oxidative pre-treatment in pure oxygen was performed before each test (10 mL min^{-1} O_2, 600 °C, 30 min). For experiments with metallic nanoparticle exsolution prior to the actual DRM experiment, an additional reducing pre-treatment in humidified H_2 was performed for one hour: pure H_2 was bubbled through a water-filled saturator at room temperature at a flow rate of 10 mL min^{-1} (leading to a H_2/H_2O ratio of ~32:1). The ideal temperature for the reducing pre-treatment was determined in previous experiments and was chosen such that exsolution of the B-site dopant occurs without decomposition of the remaining perovskite [22]. The chosen temperatures were 625 °C for the Ni-doped catalyst, 575 °C for the Co-doped material, and 700 °C for the undoped sample. The order of the "exsolution willingness" of the B-site metals – with Co at lowest temperatures followed by Ni and Fe only at the highest temperatures – is confirmed by Temperature Programmed Reduction (TPR) experiments in the SI (Fig. S6).

Afterwards, the catalyst was cooled to 400 °C in Ar (total flow of 12 mL min^{-1}). The gas phase was then changed to the reaction mixture, with flows of 3.0 mL min^{-1} CH_4, 1.5 mL min^{-1} CO_2, and 6.0 mL min^{-1} Ar (CH_4:CO_2 = 2:1). With this gas mixture, a temperature ramp from 400 °C to 700 °C with a rate of 1 °C min^{-1} was performed. In case of the purely oxidatively pre-treated samples, the temperature ramps were performed twice to check for irreversible changes during the first ramp (e.g. exsolution, deactivation). Comparing the catalytic performance directly to known materials is difficult, as quantities that could be used for such comparisons strongly depend on the experimental setup: In literature, the catalytic activity is often quantified by the conversion (a comprehensive summary of different catalysts used for DRM for a variety of different conditions and setups is given in Ref. [4]); however values one gets for conversion vary heavily with experimental

parameters (like weight of the catalyst, active surface, space time velocities…). Another quantity commonly used is the Turn Over Frequency (TOF). For this method to be applicable, however, the surface structure and number of active centres have to be known very well and should not change during the reaction [31]. As our perovskite-type oxide catalysts are dynamic systems, the number of active centres is changing under reaction conditions. Especially when exsolution occurs, it is not straightforward to determine TOF values. To account for this fact, the catalysts were compared with respect to their specific activity as outlined in previous work [19,32]. This means that the produced amount of CO was normalised to the gas flow and the surface area of the catalyst. The respective BET areas and a detailed explanation of how the calculation of the specific activity was performed can be found in the SI. For a series of high temperature measurements, a different setup was employed. A Pfeiffer PrismaPro QMG 250 mass spectrometer was used to monitor the composition. The catalysts were again pre-treated by oxidation prior to the catalytic reaction (20 mL min^{-1} O_2, 600 °C, 30 min), which was followed by a reducing pre-treatment at the respective temperature specified above (20 mL min^{-1} H_2/H_2O of ~32:1, 60 min). Afterwards, the catalyst was cooled to 400 °C in Ar and the gas atmosphere was switched to the reaction mixture. In contrast to the other catalytic experiments, the gas flow was four times higher to account for the increased activities of the catalysts at higher temperatures. For these high temperature experiments, the temperature was raised from 400 °C to 950 °C with a rate of 2 °C min^{-1}.

3. Results and discussion

3.1. Catalytic tests

Two sets of experiments were performed as catalytic tests for each catalyst: During the first set, measurements were performed immediately after an oxidising pre-treatment as described in the experimental section – samples treated that way will be designated "oxidised". For the second set, an additional reducing pre-treatment step before measurements was conducted (the corresponding samples are labelled "reduced"). These different catalysts pre-treatments led to two different starting conditions: either a fully oxidised perovskite surface or a reduced material with oxygen vacancies and exsolved nanoparticles embedded in the parent oxide. In the first case (only oxidising pre-treatment), the possibility of *in-situ* exsolution at higher DRM reaction temperatures still exists, which may lead to an increase in catalytic performance. In case of the latter experiment, exsolution already occurred during pre-reduction in H_2/H_2O, and the formed nanoparticles are present throughout the whole catalytic measurement.

For the B-site undoped sample ($Nd_{0.6}Ca_{0.4}FeO_{3-\delta}$), the catalytic results for the two experiments are shown in Figs. S1–S3 (see SI). Reduction prior to the test clearly led to an earlier onset of CO formation, with the start of CO formation being already observable at 400 °C. In contrast, the oxidised sample exhibited CO production only above 500 °C. Moreover, for the reduced sample, the CO concentration reached a first local maximum at 450 °C, before an intermediate drop. It started to rise again around 520 °C with the CO concentration constantly increasing. Interestingly, the H_2 concentration was not rising during the first CO production peak. H_2 was only produced at the highest reaction temperatures. This means, that two different processes for CO formation occur:

(i) The first CO formation peak at low temperatures took place as a consequence of the reductive pre-treatment, during which oxygen vacancies were formed in the perovskite lattice. CO_2 can react with those vacancies – refilling them while releasing CO in the process.
(ii) The second increase of the CO concentration (at higher temperatures), which also was observed in the oxidised sample, was accompanied by H_2 production. This means that at higher temperatures DRM took place.

However, as can be seen in both Fig. S1a and d in the SI, the H_2/CO ratio was not reaching the theoretical value of 1, indicating side reactions (as discussed in the introduction). The main reason for a value below 1 is that the competing rWGS reaction dominates at lower to medium temperatures. As shown in previous works, perovskite-type oxides can also be efficient for rWGS reaction [19]. The SEM images (SI, Fig. S3) taken after the catalytic reactions did not display any metallic nanoparticles for both experiments, but in case of the pre-reduced sample, particles with a diameter of more than 100 nm are visible on the surface, which were identified as $CaCO_3$. As highlighted in previous works [19], the investigated materials can form $CaCO_3$ particles at higher temperatures under CO_2-rich reaction conditions. This $CaCO_3$ phase could also be confirmed by *operando* XRD experiments, as discussed in Section 3.3 below. In Fig. S4 a SEM image with visible $CaCO_3$ crystallites is shown, and additional EDX analysis confirms their chemical nature. This formed $CaCO_3$ phase blocks catalytically active sites and, therefore, leads to deactivation of the catalyst. The difference in activity at 700 °C between the two pre-treatments was also significant as the activity increased roughly five-fold (Fig. S2a).

For the Co-doped catalyst $Nd_{0.6}Ca_{0.4}Fe_{0.9}Co_{0.1}O_{3-\delta}$, a clear activation effect of the reductive pre-treatment could be confirmed as well. CO formation started already at 400 °C with the reduced Co-doped catalyst, while in case of the oxidised perovskite the CO formation onset was at 560 °C (SI, Fig. S1b and e). The two consecutive runs for the oxidised Co-doped perovskite are nearly identical (SI, Fig. S2b), with only a slight decrease (83 % of the first run) in activity at 700 °C. A slight deactivation effect may be connected to the formation of $CaCO_3$ and CaO as seen in the *operando* XRD measurements (see Section 3.3) and in the SEM image with EDX analysis (SI, Fig. S4). The activity of the reduced sample was about one order of magnitude higher. The SEM images taken after the catalytic reaction (SI, Figs. S3a and S3d) also show a clear difference between the samples. Nanoparticles with a diameter of around 33 nm could be found on the surface of the reduced sample, while on the oxidised sample no nanoparticles could be observed.

In Fig. 2, the catalytic results for $Nd_{0.6}Ca_{0.4}Fe_{0.97}Ni_{0.03}O_{3-\delta}$ are displayed. The onset of CO production occurred at approximately 500 °C for the reduced perovskite, while the oxidised sample showed CO formation only above 550 °C. In case of the oxidised sample, a small initial increase of the CO production could be observed around 550 °C,

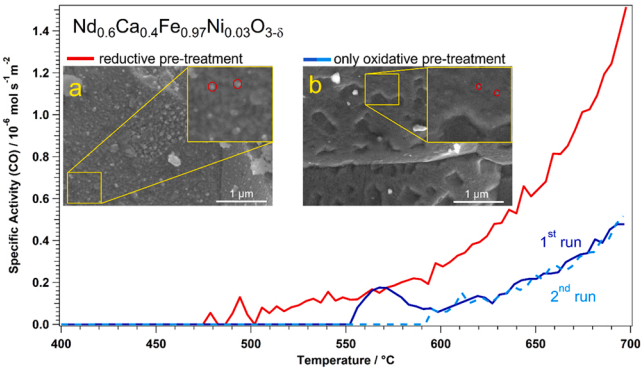

Fig. 2. Influence of the reducing pre-treatment (625 °C, 10 mL min^{-1}, wet H_2, 60 min) on the formation of nanoparticles and, subsequently, on the catalytic activity of $Nd_{0.6}Ca_{0.4}Fe_{0.97}Ni_{0.03}O_{3-\delta}$. The SEM images shown in the insets were taken after the respective reaction to check for nanoparticles. The reduced sample (red curve) showed CO production at lower temperatures and an overall greater activity. The formed nanoparticles (a) are bigger than for the oxidised sample (26 nm vs 14 nm) (b). There was no change in overall activity between the first (full dark blue line) and a second consecutive run (dashed light blue line) when the oxidised catalyst was measured a second time.

followed by a drop between 570 °C and 590 °C. This resembles the behaviour of the undoped sample; however, in this case no pre-formed oxygen vacancies were present. In this case it is a side effect of the onset of *in-situ* nanoparticle exsolution as explained in detail in the SI. Regarding the selectivity of the Ni-doped samples (Fig. S1c and f, SI), predominantly CO formation by rWGS was observed at low temperatures. Onset of significant H_2 formation via DRM was observable only at higher reaction temperatures (see also the explanation presented in Section 3.2).

The *in-situ* formation of Ni-nanoparticles could also be confirmed via SEM images taken after the catalytic experiments. In Fig. 2b, nanoparticles are shown after the runs with an oxidic pre-treatment. In contrast, the nanoparticles for the pre-reduced catalyst are substantially bigger (Fig. 2a). Their mean diameter (26 nm) was around twice the size of the particles on the oxidised catalyst (14 nm). The exact distribution of the nanoparticles is displayed in Fig. S5 (SI). The sample with bigger nanoparticles exhibited an increase in catalytic activity. These bigger nanoparticles appear to be beneficial for the activation of methane.

When comparing the three catalysts after application of reducing pre-treatments, it becomes apparent that the Ni-doped perovskite performed best with a specific activity for CO of $1.5 \bullet 10^{-6}$ mol s^{-1} m^{-2}, while the Co-doped catalyst only showed an activity of $0.75 \bullet 10^{-6}$ mol s^{-1} m^{-2}. The undoped sample exhibited an activity of only $0.37 \bullet 10^{-6}$ mol s^{-1} m^{-2}. The measurements are compared in Fig. S7 (SI).

3.2. High temperature catalytic testing

The tested perovskite catalysts exhibit significant activity with respect to the rWGS reaction at intermediate temperatures (~500–700 °C), a known competitive side reaction of DRM [19]. This causes a shift of the product ratio within this temperature range from an equal distribution to a CO excess of about 10:1 in the present study. It is, however, known that rWGS becomes less dominant for DRM applications above 800 °C [1]. As the main intention of this study was to examine the exsolution behaviour and its impact on the DRM activity, the initial focus was put on the intermediate temperature region. To get more insights into the DRM capabilities of the investigated perovskite catalysts, a second set of catalytic reactions up to 950 °C was conducted to check if the H_2/CO ratio of the product gas stream increases at higher temperatures. An overview of the results of these high temperature measurements is given in Fig. 3.

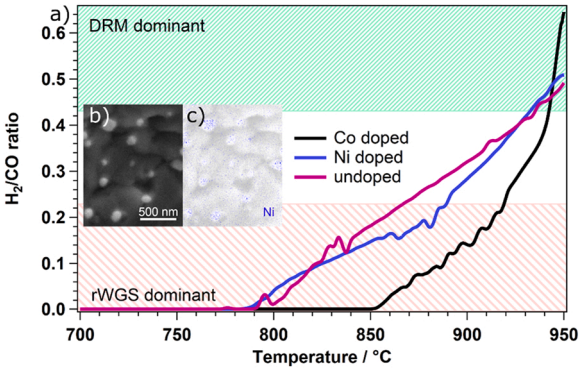

Fig. 3. Comparison of the product ratio of the reduced materials during high temperature measurements. Onset of H_2 production occurred around 790 °C in case of the undoped and the Ni-doped catalyst; the product ratio increased continuously to 0.5 for both catalysts. H_2 formation over the Co-doped catalysts starts at higher temperatures (850 °C); however, the maximum product ratio at 950 °C was higher (around 0.6). The inset shows b) a SEM image of the Ni-doped catalyst after the high temperature experiment and c) an EDX mapping of Ni (displaying the net intensity of the Ni L peak) of the same area. The particles have an average diameter of 60.9 nm and Ni accumulation within those particles is clearly visible.

During the high temperature measurements, onset of DRM occurred later than in the above-mentioned catalytic tests. This delayed onset was caused by the lower sensitivity of the MS towards low concentrations compared to the micro-GC. Also, the higher flow rates used for these experiments led to lower overall conversion. After onset of DRM, the H_2/CO ratio increased steadily up to a value of around 0.5 in case of the undoped and Ni-doped samples, and it even exceeded 0.6 for the Co-doped catalyst at 950 °C. The potential to tune the desired H_2/CO ratio by varying the composition of the perovskite lattice becomes evident. Powder XRD measurements after the reactions were performed, which confirmed that the perovskite structure was intact even after the high temperature reactions (Fig. S9, SI). Additionally, a SEM image of the used Ni-doped catalyst (Fig. 3b) shows particles with an average diameter of 60.9 nm, which is larger than in the sample that was exclusively used at lower temperatures (26 nm, cf. Fig. 2a). An EDX mapping (Fig. 3c, possible due to the larger particle size) revealed that Ni is accumulated within the particles, supporting their Ni-rich composition. It should be noted that the achieved H_2/CO ratio is still not as high as in recent literature (e.g. from Ignacio de Garcia et al. [33]). The reason for this lies in the pronounced oxygen vacancy formation and stabilisation of our perovskite oxide samples which results in a high rWGS activity and therefore decreases the H_2/CO ratio [19].

3.3. Exsolution followed by operando XRD measurements

To investigate structural changes that occur during DRM and upon *in-situ* exsolution, *operando* XRD measurements were performed. For each catalyst, experiments with both pre-formed nanoparticles and *in-situ* exsolution were conducted. For the undoped catalyst ($Nd_{0.6}Ca_{0.4}FeO_{3-\delta}$), the perovskite lattice structure (Figs. 4a as well as S11, SI) was preserved even at high temperatures and even if a reducing pre-treatment in wet H_2 was applied before reaction. This highlights the stability of the perovskite host lattice, which does not decompose under reaction conditions and holds true for the doped samples as well. However, it should be noted that exsolution as well as Ca segregation were observed meaning that the perovskite structure is a dynamic one and does undergo changes, but it remains the predominant phase. This dynamic structure, including its rich oxygen chemistry of the perovskite surface is beneficial for DRM (e.g. by preventing coking). For the undoped sample, metallic Fe formed upon pre-reduction, which was oxidised to Fe3O4 (peak at 35.4°) during DRM at lower temperatures. Between 650 °C and 700 °C, Fe3O4 was transformed back into metallic Fe (peak at 44.2°). For the oxidised sample, the formation of Fe3O4 could be observed above 550 °C, which transitioned into Fe above 650 °C as well. A comparison of the intensities of pre-reduced and oxidised samples indicates that pre-reduction led to more metallic Fe being formed during DRM (noticeable by a stronger Fe metal signal). However, in case of the pre-reduced sample, also a stronger $CaCO_3$ peak (29.4°) was observed which transformed into CaO (36.8°) above 650 °C. This may be a consequence of the more pronounced Fe exsolution; however, due to the substantially higher activity observed on the pre-reduced catalysts, a significant loss of active perovskite surface due to Ca surface segregation can be compensated. Additionally, a small diffraction peak corresponding to graphite formation was detected at 26.3° with no significant difference between the two experiments.

Fig. S12 summarises results for the Co-doped perovskite ($Nd_{0.6}Ca_{0.4}Fe_{0.9}Co_{0.1}O_{3-\delta}$) with only oxidative treatment. Exsolution of B-site elements are represented by a diffraction peak forming at 44.5°. This peak can be attributed either to a Co hcp phase or a Fe bcc phase. Alternatively, a mixed bcc phase consisting of both B-site metals is possible [34]. However, alloy formation cannot be assessed with XRD alone, as the diffraction peaks are too close to each other. The second peak of the bcc phase, located at around 64.5°, begins to form at 650 °C, which might indicate additional Fe exsolution taking place. Furthermore, the formation of $CaCO_3$, with a diffraction peak at 29.3°, could be observed starting at 550 °C. The intensity of this signal increased up to

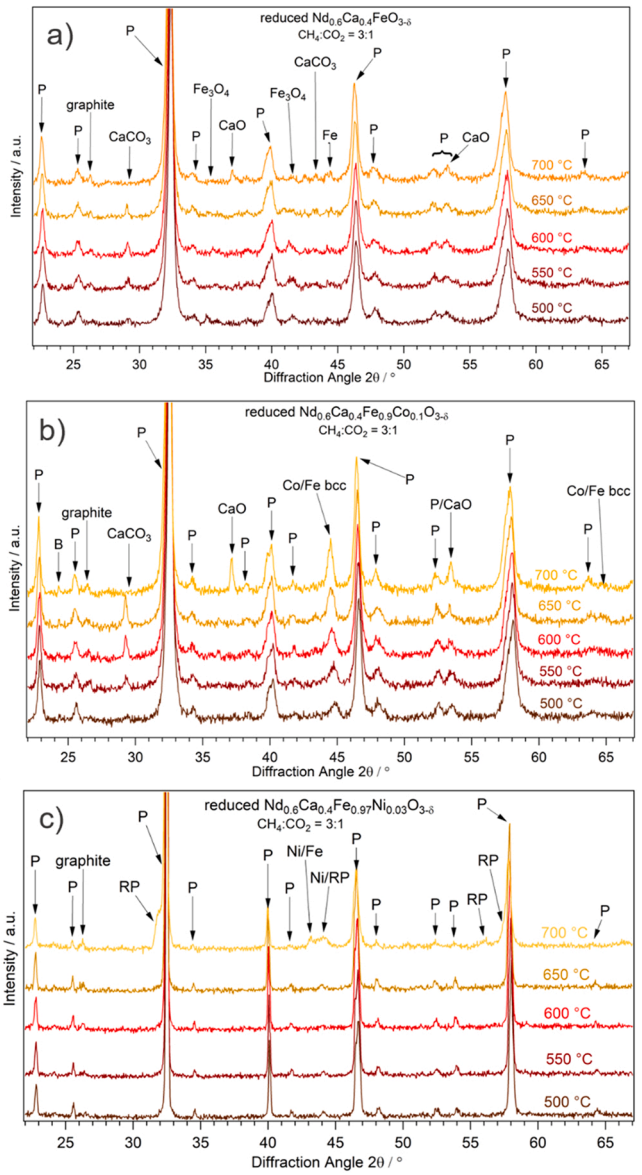

Fig. 4. Overview over the operando XRD measurements of the three pre-reduced samples: a) undoped, b) Co-doped, and c) Ni-doped in DRM atmosphere. For all materials, the diffraction peaks for the perovskite host lattice (P) remained present up to 700 °C, highlighting the stability of the catalysts. The undoped version showed the formation of a Fe_3O_4 phase while the formation of metallic dopants was visible for the doped catalysts at 550 °C (Co-doped) and 650 °C (Ni-doped), respectively.

650 °C, but it vanished at 700 °C, were $CaCO_3$ transformed into CaO, shown by the new peak at 31.2°. Even though the second peak of CaO (at 53.5°) overlaps with a perovskite peak, a change of the intensity ratios of the perovskite peaks in this region further indicated formation of CaO. Additionally, a signal corresponding to graphite started forming at 550 °C, thus indicating that at least some carbon deposition occurred. However, as the peak remained small, it can be assumed that the carbon deposition was not severe. This assumption is further supported by the fact that no CNTs could be seen in the SEM images. Alternatively, the formation of a graphite layer around the exsolved nanoparticles would be possible, but since the diffraction peak is not growing, ongoing coking was not observed. The pre-reduced sample showed similar behaviour upon heating (Fig. 4b). Exsolution was visible already at 500 °C and the corresponding diffraction peak continued to grow with rising temperature. Similar to the oxidised catalyst, Co and Fe could not be separated and appear in a combined peak at 44.5°. $CaCO_3$, CaO, and graphite were also observed.

In case of the oxidised Ni-doped catalyst ($Nd_{0.6}Ca_{0.4}Fe_{0.97}Ni_{0.03}O_{3-\delta}$, Fig. S13), sharper XRD reflexes were observed, as this sample had to be sintered at higher temperatures to achieve phase purity. In the measurement of the reduced Ni-doped catalyst, the formation of an additional phase similar to a perovskite phase was observed. At 700 °C the perovskite diffraction peaks had shoulders on their left edges (Fig. 4c). This is most likely a Ruddlesden-Popper phase (marked with "RP"). In case of the oxidised sample, peaks corresponding to Fe and Ni appear at 44.8° and 44.2°, respectively, at 650 °C. This indicates *in-situ* exsolution of the dopant and the B-site cation. The Ni particles (43.5°) on the surface of the pre-reduced sample (exsolved during the reductive pre-treatment) were observed to switch back to an oxidic state upon exposure to the DRM reaction environment at lower temperatures (i.e. the nanoparticles on the surface are oxidised). Only at higher temperatures (700 °C), the metallic state re-emerges due to the reducing reaction environment. Furthermore, a diffraction peak at 44.1° possibly corresponding to Fe is present above 500 ° in the oxidised sample. In contrast to the measurements with $Nd_{0.6}Ca_{0.4}FeO_{3-\delta}$, neither $CaCO_3$ nor CaO could be observed. In both Ni-doped samples, graphite was observed in small amounts.

Using refinement techniques, the peak widths of the undoped and the Co-doped samples were analysed. This is related to crystallite sizes, however only relative trends are reported here, as reasonable absolute quantification would require further knowledge about broadening caused by the XRD instrument. The Ni-doped perovskite (which was additionally sintered during synthesis) exhibited very narrow diffraction peaks in the XRD data (visible broadening is mainly caused by the XRD setup itself), indicating larger perovskite crystallites and high order. The broadening of the perovskite phase itself was similar (and much more pronounced than in the case of Ni-doping) for the undoped and Co-doped samples. In both cases, the catalytic reaction led to a narrowing of the perovskite phase peaks. This indicates that the pristine samples consist of relatively small perovskite crystallites, but the morphology slowly changes towards bigger and less imperfect crystallites at high reaction temperatures. Furthermore, the peak width of the metallic phase in the Co-doped sample confirms that pre-reduction led to larger crystallites (indicated by a narrower peak) – this agrees with the SEM results.

3.4. *In-situ* NAP-XPS during DRM

To further investigate the changes of the catalyst surfaces during DRM reactions, *in-situ* NAP-XPS experiments were performed. Special attention was paid to the chemical state of the elements on the B-site of the catalyst as the formation of a metallic B-site species in XPS spectra is an indicator for exsolution.

The spectroscopic results for the B-site elements for the oxidised samples are summarised in Fig. 5 (the full series is shown in the SI, Figs. S14–S16). In case of the undoped $Nd_{0.6}Ca_{0.4}FeO_{3-\delta}$, no formation of a metallic phase occurred even at 700 °C. The same experiment with the corresponding pre-reduced catalyst revealed that even at 700 °C under DRM condition or in H_2/H_2O atmosphere no Fe exsolution could be triggered (Fig. S14d).

For the oxidised Co-doped catalyst $Nd_{0.6}Ca_{0.4}Fe_{0.9}Co_{0.1}O_{3-\delta}$, the $Co2p^{3/2}$ peak exhibited a gradual shift into a metallic state (from 780.2 eV to 777.5 eV [29], Fig. S15a). First indications of a metallic Co2p contribution, corresponding to *in-situ* exsolution, were found at 500 °C. The amount of metallic species was increasing with the temperature up to 700 °C in DRM gas atmosphere. The *in-situ* pre-reduction of the catalyst revealed that metallic Co formed on the sample surface during the reduction step. When switching to DRM conditions at 400 °C, however, the Co turned oxidic again. This indicates that the formed nanoparticles are present in an oxidic form at lower temperatures. They are transformed back into a metallic state between 550 °C and 600 °C

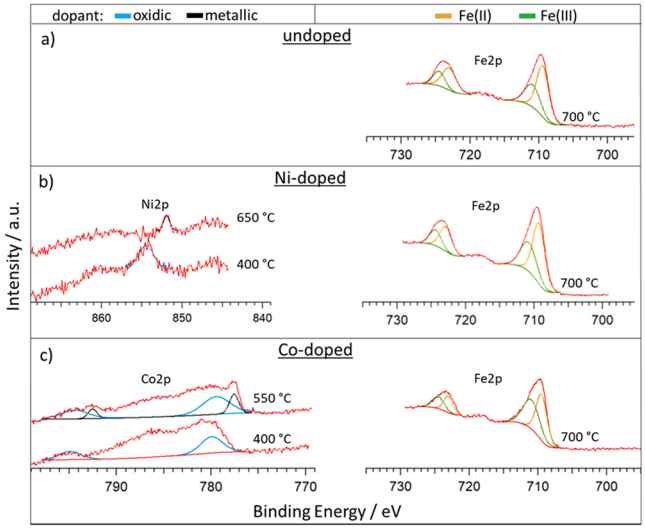

Fig. 5. Results of the *in-situ* NAP-XPS study for all oxidised catalysts during DRM (CH_4:CO_2 = 2:1, 1 mbar). The temperature was increased from 400 °C to 700 °C in 50 °C steps. Neither for the undoped $Nd_{0.6}Ca_{0.4}FeO_{3-\delta}$ (a) nor the B-site doped samples (b, c) formation of metallic Fe could be observed even at 700 °C. A metallic species should be featured prominently at around 708 eV. In case of the Ni-doped catalyst $Nd_{0.6}Ca_{0.4}Fe_{0.97}Ni_{0.03}O_{3-\delta}$ (b), a shift of the Ni2p peak could be observed between 600 °C and 650 °C indicating the formation of metallic Ni. In the XPS spectra of the Co-doped catalyst $Nd_{0.6}Ca_{0.4}Fe_{0.9}Co_{0.1}O_{3-\delta}$ (c), a second component appears at 550 °C in the Co2p spectra, that overlaps with an Fe Auger peak as shown on previous work [29]. This new component could be assigned to metallic Co. The absence of metallic Fe in both B-site doped samples indicates purely Ni- and Co-based nanoparticles, respectively.

(Fig. S15b). Interestingly, the ratio of metallic to oxidic Co is significantly larger than in the oxidised sample. This could suggest that the reductive pre-treatment led to the formation of bigger or more nanoparticles on the surface as already shown above (Fig. 2).

For the oxidised Ni-doped catalyst, a shift of the Ni2p signal was observed from the oxidic state at 854.7 eV into a metallic state at 852.2 eV between 600 °C and 650 °C (Fig. S16a) [35]. The *in-situ* measurement on the related pre-reduced catalyst demonstrated that the reduction step led to the formation of metallic Ni (Fig. S16b). Switching to DMR conditions at 400 °C caused the re-oxidation of the exsolved nanoparticles. Above 600 °C, the nanoparticles became metallic again. The Fe2p signal does not show the formation of metallic Fe during the course of any experiment (Fig. S14). This is a discrepancy to the results of the XRD measurements. Possible reasons for this are discussed in the summary.

The different behaviour between the Ni- and Co-doped catalysts, respectively, (in the Ni2p and Co2p spectra a fast switch to the metallic state within one temperature step was observed for the Ni-doped sample, while the formation of Co metal occurred more gradually in the Co-doped material) could be explained by the amount of B-site doping. Whereas the amount of Co-doping was 10 %, only 3 % Ni could successfully be incorporated into the perovskite. The Ni reservoir in the subsurface region is therefore much smaller. Thus, Ni depletes much faster upon exsolution. Moreover, remaining trace amounts of Ni within the host lattice may be below the detection limit of XPS. In case of Co-doping, the larger reservoir allows for a more gradual growth of the nanoparticles with increasing reaction temperature. The importance of the concentration of the exsolving element for exsolution properties was already proven by Gao et al. [36]. As no metallic Fe could be detected even at 700 °C, the measurements indicate that the formed nanoparticles are indeed pure Ni and Co, respectively. TPR results (shown in the SI) support that there is a temperature window, where solely the more easily reducible dopant element is reduced, while reduction of Fe starts only at even higher temperatures (the exact temperatures depend on the conditions).

The key finding of an analysis of the C1s spectra for all materials was the clear absence of dominant coking, as no strong carbon signals occurred throughout the reaction (Fig. S17). The observed carbon species were mostly present at lower temperatures and, in fact, vanished at higher reaction temperatures. According to Dama et al., the NiC_x peak, indicating the coking of the nanoparticles, forms at binding energies around 280 eV [14]. This peak was entirely absent during all measurements, and no carbonaceous structures were observed in any post-reaction SEM images, proving that all tested catalysts exhibited improved coking resistance. This is probably a consequence of the rich oxygen surface chemistry of perovskites, which hinders the formation of carbon deposits on the surface. Furthermore, it was reported that alkaline earth metals are promoting the re-oxidation of surface carbon on Ni-based catalysts [37] and Ca is known to be an exceptionally good promoter [14]. Additionally, with respect to NiC_x, Dama et al. distinguished between C-C compounds with binding energies around 285 eV and CO_x compounds with higher binding energies around 290 eV. In both these energy regions, peaks could be observed, however, no intense signal occurred, indicating that only traces of carbon were present on the surface. Concerning the C1s spectra and the carbon surface chemistry, the investigated perovskites show a quite different behaviour:

The experiment with the pre-reduced undoped catalyst ($Nd_{0.6}Ca_{0.4}FeO_{3-\delta}$) showed no C1s signals during the pre-treatments. When switching to DRM conditions, four species appeared (Fig. 6a). At ~292.5 eV, the gas phase peak becomes visible. This signal grew weaker as the temperature increased. This indicates that the CO_2 near the surface was reacting. The CO_3^{2-} species (289.2 eV) is present above 400 °C up to 700 °C. Its amount decreased with rising temperature as well. Between 285.5 eV and 286.0 eV, adventitious carbon is present; however, the signal decreased upon further heating. The species with the lowest binding energy (283.9 eV) is only visible at the 550 °C and 600 °C steps and corresponds to graphitic carbon.

The pre-reduced Co-doped catalysts displayed only two contributions to the C1s signal at lower temperatures (Fig. 6b). The carbonate species at 289.6 eV was present between 400 °C and 550 °C and vanished at higher temperatures. Adventitious carbon could be detected below 550 °C between 284.8 eV and 285.6 eV. Above 600 °C, no carbon signals could be detected.

When a reductive pre-treatment was applied to the Ni-doped catalyst, three different carbon species were visible (Fig. 6c). The species at the highest binding energy (around 292.5 eV) could be assigned to the gas phase signal. It was only visible at 400 °C and 500 °C, indicating increased CO_2 conversion at higher reaction temperatures. Between 289.3 eV and 289.7 eV, a carbonate species could be observed at the two lowest temperatures. Below 550 °C, adventitious carbon could be detected between 285.1 eV and 285.6 eV.

The O1s peak fitting revealed two relevant species (Fig. 7). The main peak, in case of all three materials between 528.3 and 528.9 eV, can be attributed to lattice oxygen of the perovskites host lattice, as reported in literature [38,39]. The smaller peak at higher binding energies consists of a carbonate component and a hydroxide component. Both of these species are important for the mechanism of DRM [40]. Even though the resolution of the lab-based XPS system is not sufficient to separate them clearly [38], the analysis of the C1s region confirms the presence of carbonate as discussed above. The signal from the C1s spectra can be used to calculate and fit the corresponding O1s contribution. The remaining peak intensity can be assigned to surface hydroxyl groups. The details for this calculation can be found in the SI (Tables S6–S12). It was observed that the carbonate amount is largest below 600 °C in each measurement. This means that surface carbonate at lower temperature most likely derives from adsorbed CO_2, which is reacting faster at higher temperatures. Alternatively, the formed $CaCO_3$ is transforming into CaO as observed in the XRD experiments (Section 3.3).

In the experiment with the undoped pre-reduced catalyst, the lattice oxygen did not shift under DRM reaction conditions; its position stayed

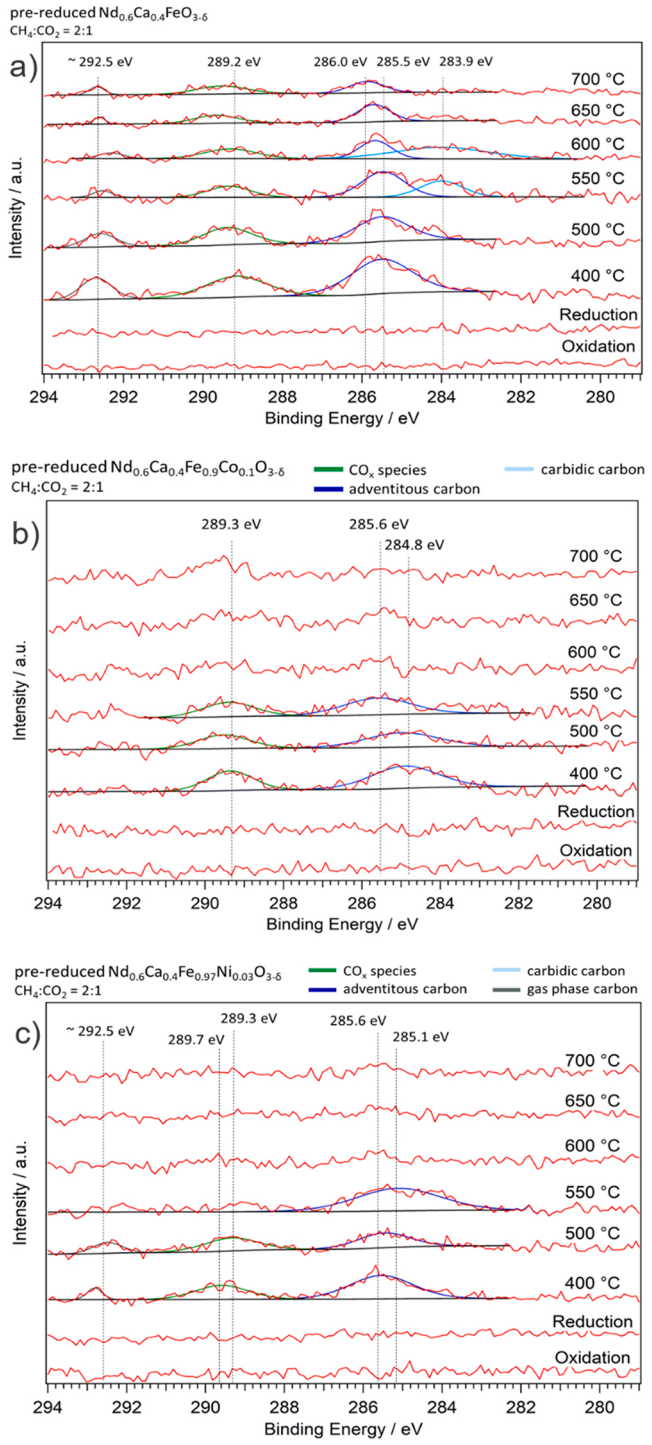

Fig. 6. Comparison of the C1s spectra of the reduced catalysts in DRM conditions – a) $Nd_{0.6}Ca_{0.4}FeO_{3-\delta}$; b) $Nd_{0.6}Ca_{0.4}Fe_{0.9}Co_{0.1}O_{3-\delta}$; c) $Nd_{0.6}Ca_{0.4}Fe_{0.97}Ni_{0.03}O_{3-\delta}$. No catalyst exhibits excessive coking and complete coverage of the surface. The carbon species found could be identified as carbonate species, adventitious carbon, graphitic carbon, and gas phase species. The detailed spectra can be found in the SI.

constant at 528.9 eV (Fig. S18d). The hydroxyl component did not shift as well and stayed at 530.4 eV [41]. Interestingly, the signal contribution assigned to the carbonate shifted to higher binding energies during reaction. As the temperature increased, the carbonate species shifted from 531.4 eV to 532.0 eV [42]. A closer look into the carbonate amount contributing to the shoulder of the main oxygen peak reveals that the carbonate amount peaks at 600 °C at 39 % (similar to the maximum amounts found for the oxidised sample as seen in Fig. S18a). In contrast to the latter, there was, however, carbonate present at higher temperatures as well. The carbonate species at lower temperatures, stemming from adsorbed CO_2, is most likely reacting similarly to the measurement with the oxidised catalyst. The carbonate remaining at higher temperatures most likely corresponds to $CaCO_3$ which was already observed in the *operando* XRD measurements.

In case of the oxidised Co-doped catalyst, the hydroxyl contribution was constant at 531.0 eV and a carbonate peak was present at 531.5 eV. Interestingly, in contrast to the undoped oxidised catalyst, carbonate is present in all measurements. The amount of carbonate in this sample was the highest for all measured catalysts. At 500 °C, the amount peaked at 64 % before declining again to around 40 % at 700 °C (Table S9). The general trend of the carbonate amount with temperature was similar to the other experiments (i.e. rising at first but declining at higher temperatures). The decrease of the amount of carbonate coincided with the temperature at which metallic Co could be observed in the measurements of the oxidised catalyst (Fig. 4). However, the Co-doped catalyst appears to exhibit a tendency to form more $CaCO_3$, as the carbonate amount on the surface was also significant at higher temperatures. During the measurement with the pre-reduced catalyst, the hydroxyl component shifted from 530.5 eV to 531.1 eV. The carbonate species was only present up to 550 °C (at 531.5 eV). As seen in Table S10 (SI), the carbonate amount remained constant at around 47 % between 400 °C and 550 °C. At higher temperatures, the carbonate amount dropped to 0, as no carbonate could be observed in the C1s region. One has to keep in mind that the areas fitted for the C1s of carbonate were already very low, the decrease of surface carbonate (through the start of DRM reaction) led to the signal dropping below the detection limit and made fitting not feasible anymore.

In case of the corresponding reduced catalyst with Ni-doping, the reductive pre-treatment caused formation of surface carbonate visible at 400 °C and 500 °C. At these temperatures, the amount of carbonate in the region with high binding energy was nearly 50 % (Fig. S18f). However, at higher temperatures (>550 °C), it completely vanishes due to the increased catalytic activity. The binding energy of the OH^- species remain unchanged at 531.0 eV during the whole measurement.

3.5. Recapitulation

The catalytic results confirm that reductive pre-treatment increased the catalytic activity significantly for all three perovskite catalysts. Compared to samples with only an oxidation step, SEM images revealed that in case of B-site doped pre-reduced perovskites the exsolved nanoparticles were significantly bigger on average, e.g. 14.1 nm compared to 25.5 nm in case of the Ni-doped perovskite, thus providing a possible explanation for the increased activity. This clearly shows that to achieve enhanced catalytic activity, pre-reduction is necessary. The Ni-doped perovskite exhibited the highest catalytic activity of all tested materials after nanoparticle exsolution. A pronounced rWGS activity could be observed at intermediate reaction temperatures. The selectivity shifts towards the desired DRM reaction only at high reaction temperatures above 800 °C. For the Ni- and Co-doped perovskites, a H_2/CO ratio of 0.5 and 0.6, respectively, could be observed at 950 °C. Kapokova et al. observed similar behaviour in their studies [43]. They reported an increase in the H_2/CO ratio with rising temperature. However, the increase in H_2 formation in that work was not as high as in our case, most likely due to the fact that perovskites used in their studies are extremely active for the rWGS reaction [19].

XRD and *operando* XRD measurements confirmed host lattice stability even at the highest reaction temperatures (950 °C) for all materials and experiments. Deactivating phases such as $CaCO_3$ and graphite were observed, but no severe coking and CNT formation as SEM images revealed. The B-site doped catalysts exhibited *in-situ* exsolution under DRM conditions – the Co-doped sample showed an exsolution onset of

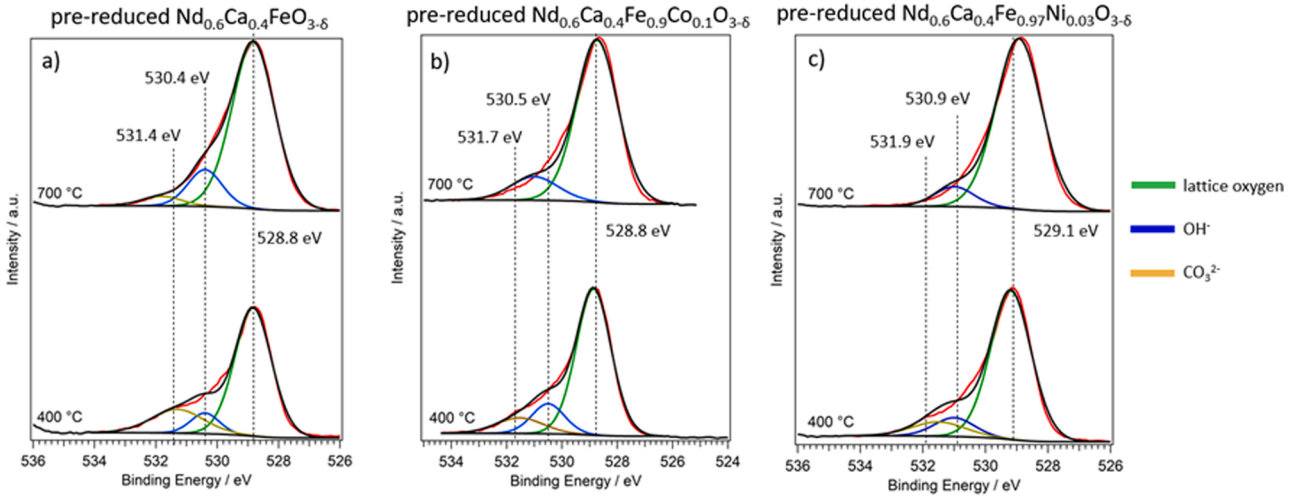

Fig. 7. Comparison between the O1s spectra of the pre-reduced catalysts (a: $Nd_{0.6}Ca_{0.4}FeO_{3-\delta}$; b: $Nd_{0.6}Ca_{0.4}Fe_{0.9}Co_{0.1}O_{3-\delta}$; c: $Nd_{0.6}Ca_{0.4}Fe_{0.97}Ni_{0.03}$ $O_{3-\delta}$) in DRM atmosphere (CH_4:CO_2 = 2:1) at 1 mbar and at 400 °C and 700 °C, respectively. The lower energy component (green) shifted very little across the measurements and can be attributed to lattice oxygen. The part of the fit at high energies (brown) corresponds to carbonate species and the medium-energy component (blue) corresponds to the hydroxide.

550 °C, exsolution on the Ni-doped material started above 600 °C.

Comparing *operando* XRD and *in-situ* NAP-XPS results, some discrepancies stand out at first glance. In the XRD results, the undoped catalyst exhibited formation of metallic Fe which could not be observed in the NAP-XPS studies. Moreover, the XRD measurements show a graphitic phase at high reaction temperatures which could not be observed in any XPS spectra. An explanation for this deviation could be the difference in the respective operating pressures: While *operando* XRD was performed at ambient pressure (1 bar), only a pressure of 1 mbar was accessible in case of NAP-XPS. This, of course, leads to different reaction rates on the surface. The pressure dependence of the chemical potential of the reaction environment plays a role as well. Additionally, more educt is reacting on the surface during *operando* XRD measurements due to larger partial pressures. This increasing reaction rate in turn leads to different rates at which oxygen vacancies are formed and side products (such as carbonaceous species) are deposited on the surface. The increased rate of the oxygen vacancy formation can, of course, cause preferred exsolution of B-site elements as a way to increase stability of the material [45]. Another difference between *operando* XRD and *in-situ* NAP-XPS is the sensitivity of the respective method. While XRD is a bulk method, XPS only probes surfaces. As it is also possible for nanoparticles to form at grain boundaries within the bulk, more exsolved metal can potentially be detected with XRD. Furthermore, two different types of samples were used for the different methods. While powders were used directly for the XRD measurements, thin film samples had to be prepared with PLD for the XPS measurements.

The graphical scheme in Fig. 8 summarises the generally accepted parts of the DRM mechanism. The scheme depicts the steps of H_2 and CO_2 activation as well as the hydrogen spill-over. The most complex and not yet fully understood step, the oxidation of the intermediates, is not shown. The formed CO_x species constitute the catalytically active carbonate species observed in the XPS measurements at lower temperatures. As mentioned above, the most complex part of the reaction mechanism is the reaction of the CO_x groups with either OH or adsorbed hydrogen to form CH_xOH, which is subsequently oxidised and desorbs as CO and H_2. For this step, a lot of different pathways can be found in the literature [20]; however, no fully agreed upon pathway has been established. Based on our findings, we propose a switch of the reaction mechanism depending on the temperature – the main property affected by this switching is the behaviour of the adsorbed hydrogen: At temperatures below 600 °C, we observed a low H_2/CO ratio, which indicates that hydrogen is not recombining to H_2, but is instead spilling over to the

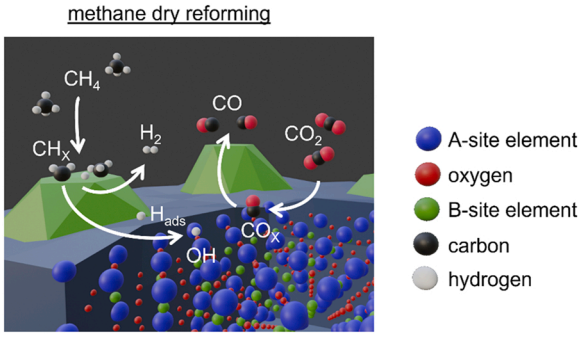

Fig. 8. Schematic overview of the catalytic processes on the perovskite surface during a DRM reaction. CH_4 is adsorbing predominantly on the exsolved nanoparticles (green) and forms CH_x adsorbents by dehydrogenation. The abstracted hydrogen can either form H_2 directly or spill over to the catalyst surface, where it forms OH-groups, which can be detected by NAP-XPS measurements. Furthermore, H_2 can react to H_2O with lattice oxygen at lower temperatures, thus creating oxygen vacancies. CO_2 is adsorbing on the oxide surface (at oxygen vacancies) where it forms carbonates (CO_x), which then desorb from the surface as CO [44].

oxide where it forms OH groups with lattice oxygen atoms. These OH groups on the surface can form water and subsequently desorb from the surface, leaving behind an oxygen vacancy that can be refilled by an adsorbed CO_2. This pathway is also shown in Fig. 1 as the "rWGS-type pathway" due to its similarity to the rWGS reaction – albeit with a different source for the adsorbed hydrogen. At higher temperatures, we observed an increase of the H_2/CO ratio which suggests a change in the system. The NAP-XPS analysis also revealed that the OH contribution in the O1s region is decreasing with rising temperature. This supports the assumption that the adsorbed hydrogen is recombining directly on the nanoparticles instead of spilling over to the support. This pathway is depicted in Fig. 1 as "DRM-type pathway".

4. Conclusion

The correlation between *in-situ* nanoparticle exsolution during DRM and exsolution by pre-reduction in wet H_2, respectively, and the subsequent catalytic performance was studied for three different perovskites: $Nd_{0.6}Ca_{0.4}FeO_{3-\delta}$ (B-site undoped), $Nd_{0.6}Ca_{0.4}Fe_{0.9}Co_{0.1}O_{3-\delta}$ (B-

site Co-doped) and $Nd_{0.6}Ca_{0.4}Fe_{0.97}Ni_{0.03}O_{3-\delta}$ (B-site Ni-doped). Although both exsolution scenarios led to the formation of Co or Ni nanoparticles on the surface of the B-site doped materials, the catalytic results show that nanoparticle exsolution by pre-reduction is enhancing the surface activity significantly more compared to *in-situ* exsolution. SEM investigations and determinations of particle size distributions reveal a possible reason for this performance difference: Nanoparticles formed during the reducing pre-treatment were bigger on average than their counterparts that were exsolved *in-situ*. At intermediate reaction temperatures, rWGS is a significant side reaction leading to reduced H_2 production. At high temperatures, the selectivity changes and DRM is the dominant pathway leading to an obtained H_2/CO ratio of 0.5 and 0.6 for the Ni- and Co-doped perovskites, respectively. These results correlate with the observed amount of hydroxyl groups on the perovskite surface (formed by H-spill over) by NAP-XPS. Of all tested perovskites, the Ni-doped catalysts showed the highest total activity.

In addition to catalytic tests, *operando* XRD and *in-situ* NAP-XPS measurements were performed during DRM. The host perovskite lattice was stable up to the highest reaction temperatures for all tested materials. Metallic phases, corresponding to the exsolved nanoparticles, could be detected by both methods in case of the B-site doped catalysts. At high reaction temperatures, the formation of trace amounts of $CaCO_3$ and graphite was observed. Both processes are undesired, as they can lead to surface deactivation. Interestingly, no formation of carbon nanotubes or big amounts of carbon deposits could be observed in case of the Ni-doped catalyst. The rich oxygen chemistry of the perovskite is a likely reason, as it facilitates effective removal of undesired carbon species, as observed by NAP-XPS.

Funding

This project has received funding from the European Research Council (ERC) under the European Union's Horizon 2020 research and innovation programme (grant agreement n° 755744 / ERC - Starting Grant TUCAS).

CRediT authorship contribution statement

Florian Schrenk: Conceptualization, Investigation, Formal analysis, Validation, Writing – original draft, Writing – review & editing. **Lorenz Lindenthal:** Investigation, Formal analysis, Visualization, Writing – review & editing. **Hedda Drexler:** Investigation, Formal analysis, Software. **Gabriele Urban:** Investigation, Formal analysis, **Raffael Rameshan:** Data curation, Investigation, Formal analysis. **Harald Summerer:** Investigation, Formal analysis, Resources. **Tobias Berger:** Investigation, Formal analysis, Software. **Thomas Ruh:** Data curation, Validation, Writing – review & editing. **Alexander K. Opitz:** Supervision, Validation, Writing – review & editing. **Christoph Rameshan:** Conceptualization, Funding acquisition, Project administration, Supervision, Writing – original draft, Writing – review & editing.

Declaration of Competing Interest

The authors declare that they have no known competing financial interests or personal relationships that could have appeared to influence the work reported in this paper.

Data availability

Data will be made available on request.

Acknowledgement

The X-ray measurements were carried out within the X-Ray Center of TU Wien; SEM images were recorded at the USTEM, TU Wien. The authors acknowledge TU Wien Bibliothek for financial support through its Open Access Funding Programme.

Appendix A. Supporting information

Supplementary data associated with this article can be found in the online version at doi:10.1016/j.apcatb.2022.121886.

References

[1] D. Pakhare, J. Spivey, A review of dry (CO_2) reforming of methane over noble metal catalysts, Chem. Soc. Rev. 43 (2014) 7813–7837.
[2] M. Behrens, Promoting the synthesis of methanol: understanding the requirements for an industrial catalyst for the conversion of CO_2, Angew. Chem. Int. Ed. 55 (2016) 14906–14908.
[3] R. Schlögl, Sustainable energy systems: the strategic role of chemical energy conversion, Top. Catal. 59 (2016) 772–786.
[4] N.A.K. Aramouni, J.G. Touma, B. Abu Tarboush, J. Zeaiter, M.N. Ahmad, Catalyst design for dry reforming of methane: analysis review, Renew. Sustain. Energy Rev. 82 (2018) 25702585.
[5] C. Rameshan, H. Li, K. Anic, M. Roiaz, V. Pramhaas, R. Rameshan, R. Blume, M. Haevecker, J. Knudsen, A. Knop-Gericke, G. Rupprechter, In situ NAP-XPS spectroscopy during methane dry reforming on ZrO_2/Pt(111) inverse model catalyst, J. Phys. Condens. Matter 30 (2018), 264007.
[6] K. Wittich, M. Kramer, N. Bottke, S.A. Schunk, Catalytic dry reforming of methane: insights from model systems, ChemCatChem 12 (2020) 2130–2147.
[7] C.E. Daza, J. Gallego, J.A. Moreno, F. Mondragon, S. Moreno, R. Molina, CO_2 reforming of methane over Ni/Mg/Al/Ce mixed oxides, Catal. Today 133 (2008) 357–366.
[8] B. Abdullah, N.A.A. Ghani, D.V.N. Vo, Recent advances in dry reforming of methane over Ni-based, Catal., J. Clean. Prod. 162 (2017) 170–185.
[9] M. Usman, W. Daud, H.F. Abbas, Dry reforming of methane: influence of process parameters—a review, Renew. Sustain. Energy Rev. 45 (2015) 710–744.
[10] M. Ocsachoque, F. Pompeo, G. Gonzalez, Rh–Ni/CeO_2–Al_2O_3 catalysts for methane dry reforming, Catal. Today 172 (2011) 226–231.
[11] Z.F. Bian, S. Das, M.H. Wai, P. Hongmanorom, S. Kawi, A review on bimetallic nickel-based catalysts for CO_2 reforming of methane, ChemPhysChem 18 (2017) 3117–3134.
[12] S.B. Wang, G.Q.M. Lu, G.J. Millar, Carbon dioxide reforming of methane to produce synthesis gas over metal-supported catalysts: state of the art, Energy Fuels 10 (1996) 896–904.
[13] M.C.J. Bradford, M.A. Vannice, CO_2 reforming of CH_4, Catal. Rev. Sci. Eng. 41 (1999) 1–42.
[14] S. Dama, S.R. Ghodke, R. Bobade, H.R. Gurav, S. Chilukuri, Active and durable alkaline earth metal substituted perovskite catalysts for dry reforming of methane, Appl. Catal. B 224 (2018) 146–158.
[15] G. Valderrama, M. Kiennemann, C.U. de Navarro, M.R. Goldwasser, $LaNi_{1-x}Mn_xO_3$ perovskite-type oxides as catalysts precursors for dry reforming of methane, Appl. Catal. A 565 (2018) 26–33.
[16] F. Touahra, R. Chebout, D. Lerari, D. Halliche, K. Bachari, Role of the nanoparticles of Cu-Co alloy derived from perovskite in dry reforming of methane, Energy 171 (2019) 465–474.
[17] Z. Lian, S.O. Olanrele, C.W. Si, M. Yang, B. Li, Critical role of interfacial sites between nickel and CeO_2 support in dry reforming of methane: revisit of reaction mechanism and origin of stability, J. Phys. Chem. C 124 (2020) 5118–5124.
[18] H. Lorenz, Q.A. Zhao, S. Turner, O.I. Lebedev, G. van Tendeloo, B. Klotzer, C. Rameshan, S. Penner, Preparation and structural characterization of SnO_2 and GeO_2 methanol steam reforming thin film model catalysts by (HR)TEM, Mater. Chem. Phys. 122 (2010) 623–629.
[19] L. Lindenthal, J. Popovic, R. Rameshan, J. Huber, F. Schrenk, T. Ruh, A. Nenning, S. Löffler, A.K. Opitz, C. Rameshan, Novel perovskite catalysts for CO_2 utilization - exsolution enhanced reverse water-gas shift activity, Appl. Catal. B 292 (2021), 120183.
[20] J.M. Wei, E. Iglesia, Isotopic and kinetic assessment of the mechanism of reactions of CH_4 with CO_2 or H_2O to form synthesis gas and carbon on nickel catalysts, J. Catal. 224 (2004) 370–383.
[21] Q. Zhao, H. Lorenz, S. Turner, O.I. Lebedev, G. Van Tendeloo, C. Rameshan, B. Klotzer, J. Konzett, S. Penner, Catalytic characterization of pure SnO_2 and GeO_2 in methanol steam reforming, Appl. Catal. A 375 (2010) 188–195.
[22] L. Lindenthal, T. Ruh, R. Rameshan, H. Summerer, A. Nenning, C. Herzig, S. Loffler, A. Limbeck, A.K. Opitz, P. Blaha, C. Rameshan, Ca-doped rare earth perovskite materials for tailored exsolution of metal nanoparticles, Acta Cryst. B 76 (2020) 1055–1070.
[23] D. Neagu, T.S. Oh, D.N. Miller, H. Menard, S.M. Bukhari, S.R. Gamble, R.J. Gorte, J.M. Vohs, J.T.S. Irvine, Nano-socketed nickel particles with enhanced coking resistance grown in situ by redox exsolution, Nat. Commun. 6 (2015) 8120.
[24] L. Lindenthal, R. Rameshan, H. Summerer, T. Ruh, J. Popovic, A. Nenning, S. Loffler, A.K. Opitz, P. Blaha, C. Rameshan, Modifying the surface structure of perovskite-based catalysts by nanoparticle exsolution, Catalysts 10 (2020) 268–281.
[25] M. Nemeth, Z. Schay, D. Sranko, J. Karolyi, G. Safran, I. Sajo, A. Horvath, Impregnated Ni/ZrO_2 and Pt/ZrO_2 catalysts in dry reforming of methane: activity tests in excess methane and mechanistic studies with labeled $^{13}CO_2$, Appl. Catal. A 504 (2015) 608–620.

[26] A. Izquierdo-Colorado, R. Debek, P. Da Costa, M.E. Galvez, Excess-methane dry and oxidative reforming on Ni-containing hydrotalcite-derived catalysts for biogas upgrading into synthesis gas, Int. J. Hydrog. Energy 43 (2018) 11981–11989.
[27] ICDD, PDF-4+2019, S. Kabekkodu (Ed.), International Centre for Diffraction Data, Newtown Square, PA, USA, 2018.
[28] T. Degen, M. Sadki, E. Bron, U. Konig, G. Nenert, The HighScore suite, Powder Diffr. 29 (2014) S13–S18.
[29] R. Rameshan, A. Nenning, J. Raschhofer, L. Lindenthal, T. Ruh, H. Summerer, A. K. Opitz, T.M. Huber, C. Rameshan, Novel sample-stage for combined near abmient pressure X-ray photoelectron spectroscopy catalytic characterization and electrochemical impendance spectroscopy, Crystals 10 (2020) 947–962.
[30] C. Ahamer, A.K. Opitz, G.M. Rupp, J. Fleig, Revisiting the temperature dependent ionic conductivity of yttria stabilized zirconia (YSZ), J. Electrochem. Soc. 164 (2017) F790–F803.
[31] F. Schuth, M.D. Ward, J.M. Buriak, Common pitfalls of catalysis manuscripts submitted to chemistry of materials, Chem. Mater. 30 (2018) 3599–3600.
[32] J. Popovic, L. Lindenthal, R. Rameshan, T. Ruh, A. Nenning, S. Loffler, A.K. Opitz, C. Rameshan, High temperature water gas shift reactivity of novel perovskite catalysts, Catalysts 10 (2020) 582–598.
[33] I.D. Garcia, A. Stankiewicz, H. Nigar, Syngas production via microwave-assisted dry reforming of methane, Catal. Today 362 (2021) 72–80.
[34] K. Gandha, P.C. Tsai, G. Chaubey, N. Poudyal, K. Elkins, J. Cui, J.P. Liu, Synthesis and characterization of FeCo nanowires with high coercivity, Nanotechnology 26 (2015), 075601.
[35] C.P. Li, A. Proctor, D.M. Hercules, Curve fitting analysis of ESCA Ni 2p spectra of nickel-oxygen compounds and Ni/Al_2O_3 catalysts, Appl. Spectrosc. 38 (1984) 880–886.
[36] Y. Gao, D.J. Chen, M. Saccoccio, Z.H. Lu, F. Ciucci, From material design to mechanism study: nanoscale Ni exsolution on a highly active A-site deficient anode material for solid oxide fuel cells, Nano Energy 27 (2016) 499–508.
[37] E. Ruckenstein, Y.H. Hu, Carbon dioxide reforming of methane over nickel alkaline earth metal oxide catalysts, Appl. Catal. A 133 (1995) 149–161.
[38] J. Requies, M.A. Cabrero, V.L. Barrio, M.B. Guemez, J.F. Cambra, P.L. Arias, F. J. Perez-Alonso, M. Ojeda, M.A. Pena, J.L.G. Fierro, Partial oxidation of methane to syngas over Ni/MgO and Ni/La_2O_3 catalysts, Appl. Catal. A 289 (2005) 214–223.
[39] A.K. Opitz, C. Rameshan, M. Kubicek, G.M. Rupp, A. Nenning, T. Goetsch, R. Blume, M. Haevecker, A. Knop-Gericke, G. Rupprechter, B. Kloetzer, J. Fleig, The chemical evolution of the $La_{0.6}Sr_{0.4}CoO_{3-\delta}$ surface under SOFC operating conditions and its implications for electrochemical oxygen exchange activity, Top. Catal. 61 (2018) 2129–2141.
[40] C. Papadopoulou, H. Matralis, X. Verykios, Utilization of biogas as a renewable carbon source: dry reforming of methane, in: L. Guczi, A. Erdôhelyi (Eds.), Catalysis for Alternative Energy Generation, Springer, New York, 2012, 57–127.
[41] J.C. Dupin, D. Gonbeau, P. Vinatier, A. Levasseur, Systematic XPS studies of metal oxides, hydroxides and peroxides, Phys. Chem. Chem. Phys. 2 (2000) 1319–1324.
[42] J. Stoch, J. Gablankowskakukucz, The effect of carbonate contaminations on the XPS O 1s band structure in metal oxides, Surf. Interface Anal. 17 (1991) 165–167.
[43] L. Kapokova, S. Pavlova, R. Bunina, G. Alikina, T. Krieger, A. Ishchenko, V. Rogov, V. Sadykov, Dry reforming of methane over $LnFe_{0.7}Ni_{0.3}O_{3-\delta}$ perovskites: influence of Ln nature, Catal. Today 164 (2011) 227–233.
[44] J.H. Bitter, K. Seshan, J.A. Lercher, Mono and bifunctional pathways of CO_2/CH_4 reforming over Pt and Rh based catalysts, J. Catal. 176 (1998) 93–101.
[45] O. Kwon, S. Sengodan, K. Kim, G. Kim, H.Y. Jeong, J. Shin, Y.W. Ju, J.W. Han, Exsolution trends and co-segregation aspects of self-grown catalyst nanoparticles in perovskites, Nat. Commun. 8 (2017) 15967.